01 May 2014

Flexoelectricity and Ferroelectric Domain Wall Structures: Phase-Field Modeling and DFT Calculations

Yijia Gu
Missouri University of Science and Technology, guyij@mst.edu

Menglei Li

Anna N. Morozovska

Yi Wang

et. al. For a complete list of authors, see https://scholarsmine.mst.edu/matsci_eng_facwork/2478

Recommended Citation

Y. Gu et al., "Flexoelectricity and Ferroelectric Domain Wall Structures: Phase-Field Modeling and DFT Calculations," *Physical Review B - Condensed Matter and Materials Physics*, vol. 89, no. 17, American Physical Society (APS), May 2014.
The definitive version is available at https://doi.org/10.1103/PhysRevB.89.174111

Flexoelectricity and ferroelectric domain wall structures: Phase-field modeling and DFT calculations

Yijia Gu,[1] Menglei Li,[1,2] Anna N. Morozovska,[3,4] Yi Wang,[1] Eugene A. Eliseev,[4]
Venkatraman Gopalan,[1] and Long-Qing Chen[1]

[1]*Department of Materials Science and Engineering, Pennsylvania State University, University Park, Pennsylvania 16802, USA*
[2]*Department of Physics and State Key Laboratory of Low-Dimensional Quantum Physics, Tsinghua University, Beijing 100084, People's Republic of China*
[3]*Institute of Physics, National Academy of Science of Ukraine, 46, pr. Nauki, 03028 Kiev, Ukraine*
[4]*Institute for Problems of Materials Science, National Academy of Science of Ukraine, Krjijanovskogo 3, 03142 Kiev, Ukraine*

(Received 5 October 2013; published 27 May 2014)

We show that flexoelectric effect is responsible for the non-Ising character of a 180° ferroelectric domain wall. The wall, long considered being of Ising type, contains both Bloch- and Néel-type polarization components. Using the example of classic ferroelectric $BaTiO_3$, and by incorporating the flexoelectric effect into a phase-field model, it is demonstrated that the flexoelectric effect arising from stress inhomogeneity around the domain wall leads to the additional Bloch and Néel polarization components. The magnitudes of these additional components are two or three magnitudes smaller than the Ising component, and they are determined by the competing depolarization and flexoelectric fields. Our results from phase-field model are consistent with the atomistic scale calculations. The results prove the critical role of flexoelectricity in defining the internal structure of ferroelectric domain walls.

DOI: 10.1103/PhysRevB.89.174111 PACS number(s): 77.80.Dj, 77.65.−j, 77.84.Cg

I. INTRODUCTION

The coupling between electric polarization (P_i) and mechanical deformation strain (ε_{ij}) is a fundamental property of materials. With zero electric field, this coupling in first order can be written as

$$P_i = d_{ijk}\varepsilon_{jk} + \mu_{ijkl}\frac{\partial \varepsilon_{kl}}{\partial x_j} \quad (i,j,k,l = 1,2,3), \tag{1}$$

where d_{ijk} is third-rank piezoelectric tensor and μ_{ijkl} is known as the fourth-rank flexoelectric (polarization) tensor. The first term on the right-hand side of Eq. (1) describes piezoelectric contribution, the linear coupling of polarization and strain, and is present only in materials that lack inversion symmetry. The second term is the flexoelectric contribution, which is a linear dependence of the polarization on strain gradient, and is present in all materials. For example, $SrTiO_3$ and NaCl are not piezoelectric, but they are flexoelectric. Albeit ubiquitous, the flexoelectric effect is usually ignored. This is because the flexoelectric coefficients, μ_{ijkl}, are very small, typically on the order of nC/m [1]. However, when the system size scales down to nanometer scale, the strain gradients can reach $\sim 10^8$ m^{-1}, and thus this effect can become significant or even dominate. The domain walls, which have strain variation and thickness on the nanometer scale, are excellent candidates for displaying significant flexoelectricity.

The antiparallel (180°) domain wall is one of the simplest and is universally present in all ferroelectrics. The spontaneous polarizations in the neighboring domains are both parallel to the domain wall but along opposite directions. It has long been believed that this type of domain wall is Ising-like, as shown in Fig. 1(a). However, recent theoretical studies have found that they are more complex. First-principles calculations showed that the 180° domain wall of tetragonal $BaTiO_3$ is Ising-like, with fluctuations in the polarization component perpendicular to the domain wall that did not appear to be spatially correlated with the wall; they were thus dismissed as artifacts [2]. Also using first-principles theory, Lee *et al.* [3] first showed that the 180° domain wall of $LiNbO_3$ and $PbTiO_3$ indeed possessed non-Ising characters. The trigonal $LiNbO_3$ exhibits both Bloch-like and Néel-like polarization components [3]. The antiparallel wall in tetragonal $PbTiO_3$ exhibits an Ising-Néel-like polarization configuration [3] [Fig. 1(b)] and additional Bloch-Néel-like features by changing the domain wall orientation [4]. A Landau-Ginzburg-Devonshire (LGD) theoretical analysis demonstrated that the 180° domain walls of tetragonal $BaTiO_3$ are bichiral, i.e., two orthogonal polarization components parallel to the wall [[5]; Fig. 1(c)]. From all these theoretical calculations, we conclude that the 180° domain walls are predominantly Ising-like, but mixed with Bloch- and/or Néel-like fluctuations. However, among all these theoretical works, only Ref. [5] studied the origin of the non-Ising features. Based on the LGD continuum model, they found that the Bloch-like characteristic is due to the flexoelectric effect. However, the Néel-like feature was neglected by Ref. [5], although the authors indicated it may originate from flexoelectric effect also. In addition, it is still unknown whether the results from the continuum model [5] are consistent with those from the atomic scale calculations [2–4]. Hence, a systematic study, which can bridge these calculations from two different scales, consolidate all the non-Ising features, and more importantly reveal the underlining mechanism for them, is needed.

Assuming the electric polarization comes from the displacements of Ti^{4+} and O^{2-}, a 180° domain wall of tetragonal $BaTiO_3$ is sketched in Fig. 1(d). The domain wall plane lies on a Ba-O plane, and the neighboring two domains have out-of-plane spontaneous polarizations antiparallel to each other. Due to the mirror symmetry, the oxygen atoms on the wall plane are not displaced, which induces the deformation with respect to the stress-free equilibrium tetragonal unit cell. Since the deformation is confined to the domain wall region that is less than 1 nm thick, the strain gradient generated from the domain wall can reach as high as $\sim 10^7$–10^8 m^{-1}. Thus,

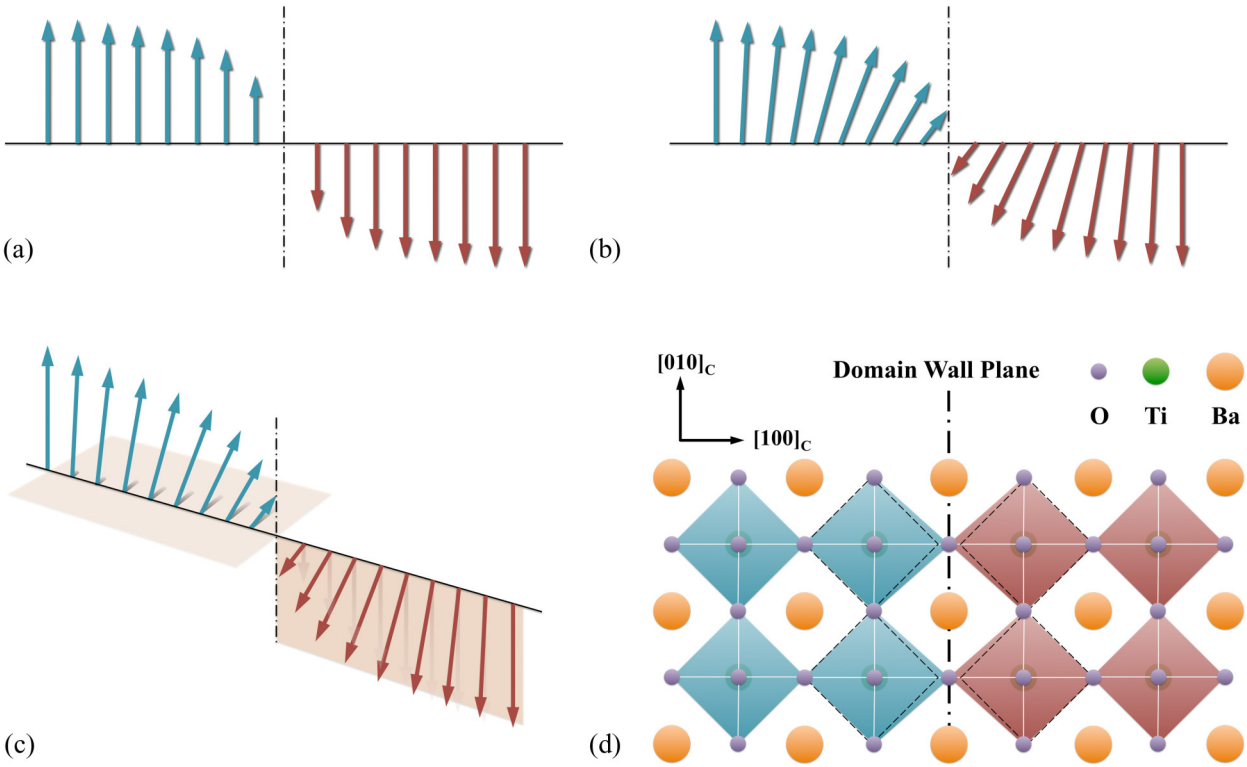

FIG. 1. (Color online) (a) Ising-type domain wall. The blue and red arrows represent positive and negative polarizations, respectively. (b) Ising-Néel-like domain wall. (c) Ising-Bloch-like domain wall. (d) The schematic of the 180° domain wall in tetragonal $BaTiO_3$. The blue and red oxygen octahedra indicate positive and negative out-of-plane polarizations, respectively. The adjacent unit cells at the wall are deformed as indicated by the dashed squares.

simply from Eq. (1), the additional polarization induced by flexoelectric effect is on the magnitude of 10^{-2} C/m^2, which should be considered (the spontaneous polarization of $BaTiO_3$ at room temperature is 0.26 C/m^2). But how significant is the induced polarization, especially the component normal to the wall (Néel feature), which may be greatly suppressed by the depolarization field [5]? And what are the new features of the polarization induced by the flexoelectric effect at the domain walls where bulk symmetry is broken? In this paper, we demonstrate that the 180° domain wall structure of tetragonal perovskite $BaTiO_3$ has both Bloch-like and Néel-like features. Both features are found to be strongly anisotropic. Previously reported calculations either missed [3] or neglected [5] one of the two components. By using a combination of phase-field modeling [6,7] and first-principles calculations, we show that the additional Bloch-Néel-like feature is intrinsic to a 180° domain wall and is entirely due to the flexoelectric effect.

II. NON-ISING CHARACTERS OF THE FERROELECTRIC DOMAIN WALL

We first extended the phase-field model of ferroelectric domains [6,7] to include the flexoelectric contributions. According to LGD theory, the Gibbs free energy of a ferroelectric crystal is given by [8]

$$G = \alpha_{ij}P_iP_j + \alpha_{ijkl}P_iP_jP_kP_l + \alpha_{ijklmn}P_iP_jP_kP_lP_mP_n + \alpha_{ijklmnor}P_iP_jP_kP_lP_mP_nP_oP_r + \frac{1}{2}g_{ijkl}\frac{\partial P_i}{\partial x_j}\frac{\partial P_k}{\partial x_l} - \frac{1}{2}s_{ijkl}\sigma_{ij}\sigma_{kl} - Q_{ijkl}\sigma_{ij}P_kP_l + \frac{F_{ijkl}}{2}\left(\frac{\partial P_K}{\partial x_l}\sigma_{ij} - \frac{\partial P_{ij}}{\partial x_l}P_k\right) - P_i\left(E_i + \frac{E_i^d}{2}\right), \quad (2)$$

where x_i is the ith component of the Cartesian coordinate system, P_i is the polarization component, σ_{ij} is the stress component, E_i is the applied electric field, E_i^d is the depolarization field, α's are the dielectric stiffness tensor (only α_{ij} is assumed to be temperature dependent), g_{ijkl} is the gradient energy coefficient, s_{ijkl} is the elastic compliance tensor, Q_{ijkl} is the electrostrictive tensor, and F_{ijkl} is the flexoelectric tensor. The values of the coefficients for $BaTiO_3$ are from the literature [9–12], as listed in Table I.

We then theoretically studied the orientation dependence of a 180° wall. The setup of the system is illustrated in Fig. 2 schematically, with the angle θ representing the rotation angle of the domain wall with respect to the crystallographic direction $[100]_C$. The subscript C denotes the original

TABLE I. Material parameters of $BaTiO_3$.

Coefficients	Values (collected and recalculated mainly from Ref. [10])
ε_b, ε_0	$\varepsilon_b = 45$ (Ref. [12]), $\varepsilon_0 = 8.85 \times 10^{-12}$ F/m
a_i ($C^{-2}\cdot m\cdot J$)	$a_1^C = 5 \times 10^5 T_S\left(\mathrm{Coth}\left(\frac{T_S}{T}\right) - \mathrm{Coth}\left(\frac{T_S}{390}\right)\right)$, $T_S = 160$ K (at 293 K $a_1^C = -4.277 \times 10^7$)
a_{ij} ($\times 10^8$ $C^{-4}\cdot m^5\cdot J$)	$a_{11}^C = -1.154$, $a_{12}^C = 6.53$
a_{ijk} ($\times 10^9$ $C^{-6}\cdot m^9\cdot J$)	$a_{111}^C = -2.106$, $a_{112}^C = 4.091$, $a_{123}^C = -6.688$
a_{ijkl} ($\times 10^{10}$ $C^{-8}\cdot m^{13}\cdot J$)	$a_{1111}^C = 7.59$, $a_{1112}^C = -2.193$, $a_{1122}^C = -2.221$, $a_{1123}^C = 2.416$
Q_{ij} ($C^{-2}\cdot m^4$)	$Q_{11}^C = 0.11$, $Q_{12}^C = -0.045$, $Q_{44}^C = 0.059$
s_{ij} ($\times 10^{-12}$ Pa^{-1})	$s_{11}^C = 9.07$, $s_{12}^C = -3.19$, $s_{44}^C = 8.2$
g_{ij} ($\times 10^{-10}$ $C^{-2}\cdot m^3\cdot J$)	$g_{11}^C = 5.1$, $g_{12}^C = -0.2$, $g_{44}^C = 0.2$ [11]
F_{ij} ($\times 10^{-11}$ $C^{-1}\cdot m^3$)	$F_{11}^C = 0.3094$, $F_{12}^C = -0.279$, $F_{44}^C = -0.1335$ (recalculated from Ref. [9])

crystallographic coordinate of pseudocubic lattice. The domain wall lies in the x_2-x_3 plane and perpendicular to the x_1 direction. The system is then simplified to a one-dimensional problem with the simulation size $4096\Delta x \times 1\Delta x \times 1\Delta x$ using the three-dimensional phase-field model. Periodical boundary condition is imposed along each direction. The stress of each grid point is calculated using Kachaturyan's microelastic theory [13], and the electric depolarization field is obtained by solving Poisson's equation. For the one-dimensional case, the depolarization field is simply $-P_1/(\varepsilon_b\varepsilon_0)$, where ε_b and ε_0 are the dielectric constant of background [12,14,15] and vacuum permittivity, respectively. We start from a two-domain structure with only spontaneous $+P_3$ and $-P_3$ in each domain, as illustrated in Fig. 2, and then let the system relax to equilibrium.

To check the existence of the Néel feature, we first calculated the polarization profile of the 180° domain wall at $\theta = 0$ [$(100)_C$ plane], as shown in Fig. 3(a). In addition to the P_3 component, we observe nonzero antiferroelectriclike P_1 component perpendicular to the domain walls, while the P_2 component remains exactly zero after relaxation. The calculated polarization profile is very similar to Lee's atomistic

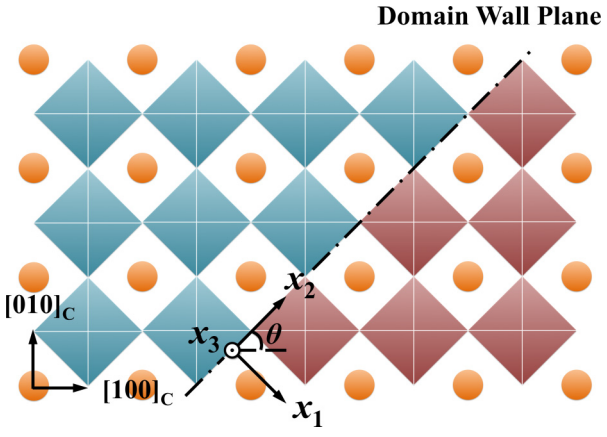

FIG. 2. (Color online) The system setup for the phase-field simulations of 180° ferroelectric domain walls in tetragonal $BaTiO_3$. Subscript C denotes the crystallographic direction. x_2 and x_3 directions are parallel to the domain wall plane, while x_1 is always perpendicular to the wall. θ indicates the angle between domain wall and the crystallographic direction $[100]_C$.

calculations of the 180° domain wall in tetragonal $PbTiO_3$ [3]. We have carefully checked that although the magnitude of P_1 is small, it is not the artifact of the numerical calculation. (A detailed analysis of possible sensitivity of polarization component on various parameters is shown in the Appendix.)

To validate our results with theoretical calculations from the atomic level, we also performed first-principles calculations as shown in Fig. 3(b). The computed bulk $BaTiO_3$ structural parameters in the tetragonal phase were $a = 3.9799$ Å and $c = 4.0768$ Å, which are very close to the experimental values of $a = 3.9970$ Å and $c = 4.0314$ Å [16]. We stacked the five-atom unit cells in the x_1 direction to form a supercell consisting of $2N \times 1 \times 1$ ($N = 4, 5, \ldots, 8$) unit cells and made half of the N cells have initial polarizations P_3 pointing up and the other half pointing down. But the atoms at the domain wall were maintained at centrosymmetric positions to ensure the mirror symmetry, thus the supercell has the similar two-domain structure as the phase-field simulation. The calculations converged well for $N > 5$. Besides the situation where the $(100)_C$ domain wall lies on the Ba-O plane, as in the phase-field modeling, a 180° wall can also be centered on the Ti-O plane. Both a previous study [17] and our calculations show that the BaO-centered domain walls are more stable. Therefore, it is reasonable to focus only on the BaO-centered $(100)_C$ domain wall. The local polarizations were calculated using the method of Meyer and Vanderbilt [17]. During the structure relaxation, we fixed the two lattice vectors parallel to the domain wall plane and optimized the third lattice vector normal to the plane in order to eliminate the influence of the elastic energy. After the structure relaxation under Ba-centered inversion symmetry constraints, the P_1 component emerged while the P_2 component remained zero. The spontaneous polarization P_3 calculated from first-principles is around 0.31 C/m^2 [Fig. 3(b)], which is consistent with the 0 K value of tetragonal phase extrapolated from the phase-field model. Although the width of Néel wall may not be accurate (affected by the short period of the computational cell), the profile of P_1 shows an antiferroelectriclike distribution with the peak appearing at the first unit cell, which is in good agreement with the phase-field result. It should be mentioned that the magnitudes of P_1 calculated from these two methods are about three times different. The discrepancy may be due to the limitation of the continuum LGD theory, i.e., the higher order polarization gradient terms or nonlinear elasticicity may

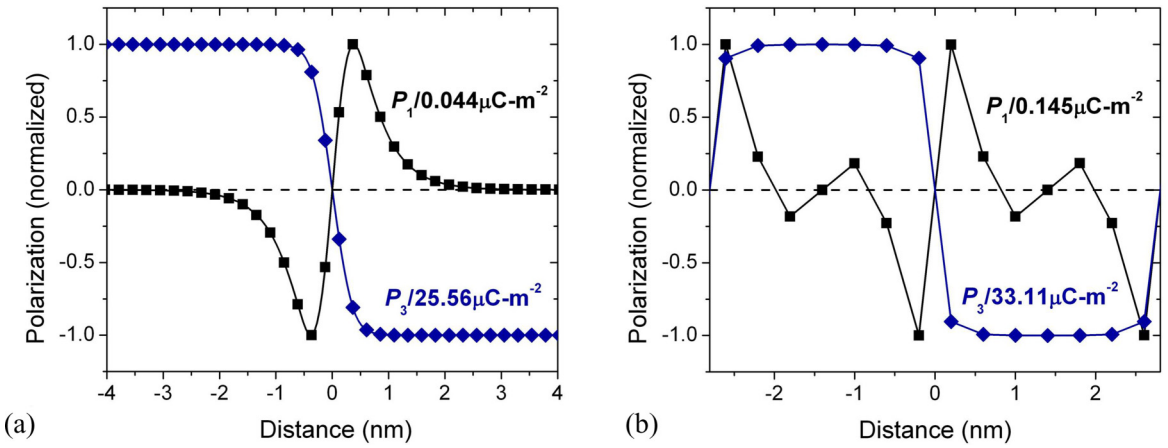

FIG. 3. (Color online) (a) The phase-field simulation result of the 180° domain wall profile in tetragonal $BaTiO_3$ at $\theta = 0$. In addition to the conventional Ising wall, a Néel-type component is also observed. (b) Polarization profile calculated from first-principles calculations. The plot shows a period of the computation cell with two domain walls.

become important at such a small scale. Meanwhile, the results from first-principles calculations are for 0 K, which are usually larger than room temperture values. Thus the first-principles calculations qualitatively agree with phase-field results and confirm that the 180° domain wall at $\theta = 0$ is Ising-Néel-like.

Comparing the results with the previous model suggests that the additional flexoelectric contribution leads to the appearance of the Néel-like feature. To convincingly validate our hypothesis, we performed phase-field simulations with the flexoelectric effect turned off. Indeed, at equilibrium, there only exists a P_3 component in the system, which has the same profile as shown in Fig. 2(a). Therefore, we conclude that the appearance of P_1 is entirely driven by the flexoelectric effect due to stress inhomogeneity around the domain walls.

As shown in Fig. 3, the induced P_1 component shows a tail-to-tail configuration, which may result in a negative bound charge and thus influence the conductivity of the wall. However, from the phase-field simulation, we found the electric potential change at the domain wall is very weak, on the order of 10^{-3} V. The bound charge at the wall center is very low, $\sim 10^6$ C/m^3, and the overall charge around the wall is zero. So the wall remains charge-neutral if the total charge is averaged across the domain wall thickness.

The domain wall orientation, which affects both the strain gradient and the flexoelectric coefficients, further complicates the character of ferroelectric domain walls. As θ changes from 0 to 2π, the phase-field simulations show that P_2 becomes nonzero as well. The maximum values of P_1 and P_2 as a function of rotation angle θ are plotted in Fig. 4(d). The P_1 component has nonzero values at all angles, while the P_2 component is zero when $\theta = n\pi/4$ (n is an arbitrary integer). In other words, the pure ferroelectric domain wall is an Ising-Néel wall when $\theta = n\pi/4$ and is an Ising-Bloch-Néel wall for all other orientations. It should be mentioned that the P_2 profile plotted in Fig. 4(d) agrees very well with Ref. [5] in terms of profile shape and magnitude.

As an example, Figs. 4(a) and 4(b) compare the domain wall profile of oblique walls with $\theta = 5\pi/12$ and $\theta = \pi/12$. Both P_1 and P_2 show antiferroelectriclike distributions, i.e., they are antiparallel near the domain walls, but vanish at the wall center. The profiles of all the polarization components are odd functions, and they agree quite well with previous calculations [3,5,18] in magnitude and profile shape. Figure 4(c) shows the result from first-principles calculations with $\theta \approx 5\pi/12$. We obtain this domain wall structure by expanding the dimensions of the single domain to $\sqrt{17}a \times \sqrt{17}a \times c$ and by putting two such domains of opposite P_3 polarizations together along the x_1 direction. Thus the domain wall actually lies in the $(410)_C$ plane. Similar to the $(100)_C$ domain wall, we only consider the O-Ba-O plane as the centered wall. Also, as we dealt with the $(100)_C$ domain wall, we relaxed this configuration with symmetry constraints and optimized the length of the normal-to-wall lattice vector. After the geometry optimization, both P_1 and P_2 are nonzero. Again the polarization components from first-principles method are larger than those calculated from phase-field method, but the peak positions are very close. Qualitatively, both computational methods confirm that the 180° domain wall is Ising-Bloch-Néel-like when $\theta \neq n\pi/4$.

III. THE FEATURES OF NON-ISING CHARACTERS

The flexoelectric effect induced polarization components exhibit unique properties. An interesting feature among them is the chirality of P_1 and P_2 profiles as shown in Fig. 4(a) and 4(b). First, three polarization components seem to be independent of each other. This can be simply explained by the small magnitude of P_1 and P_2. Second, the profile of P_2 flips when the rotation angle goes from θ to its complementary angle $\pi/2 - \theta$, while chirality of the Néel wall is apparently independent of rotation angle θ. This means that the Néel wall is always tail-to-tail regardless of the wall orientation. We will demonstrate below that the chirality can be explained within the framework of LGD analytical theory by including the flexoelectric effect.

By minimizing the total free energy [Eq. (2)], we get the equations of state

$$g_{ijkl}\frac{\partial^2 P_k}{\partial x_j \partial x_l} = 2\alpha_{ij}P_j - Q_{ijkl}P_j\sigma_{kl} - F_{ijkl}\frac{\partial \sigma_{kl}}{\partial x_j} - E_i^d, \quad (3)$$

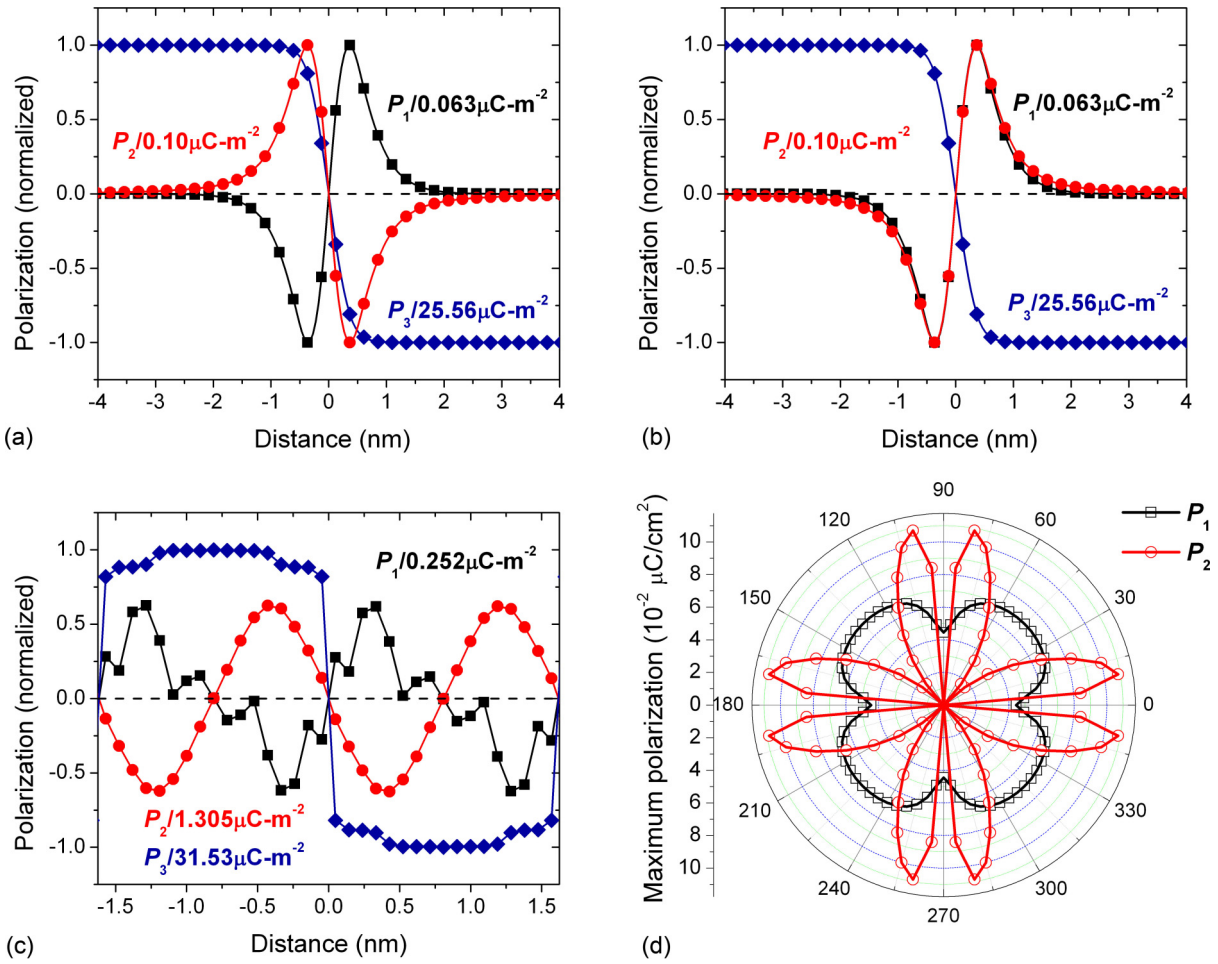

FIG. 4. (Color online) Polarization profiles of 180° domain walls. (a) P_1 and P_2 distribution at $\theta = 5\pi/12$ and (b) at $\theta = \pi/12$ from the phase-field method. P_1 remains identical while P_2 flips with θ. Both P_1 and P_2 are independent of P_3. (c) P_1 and P_2 profiles at $\theta \approx 5\pi/12$ from first-principles calculations. (d) Maximum absolute value of the polarization components induced by the flexoelectric effect in the wall as a function of the rotation angle θ, calculated from the phase-field method.

where $F_{ijkl} = s_{ijmn} f_{mnkl}$ is the flexoelectric field coefficient [19]. (Higher order terms in P polynomials are ignored for simplicity.) The first two terms on the right-hand side are small at the domain walls (see the first part of the Appendix for details). Equation (3) can be further reduced to

$$g_{ijkl} \frac{\partial^2 P_k}{\partial x_j \partial x_l} = -E_i^f - E_i^d, \tag{4}$$

where $E_i^f = F_{ijkl} \frac{\partial \sigma_{kl}}{\partial x_j}$ is the so-called flexoelectric field [19], which is used to describe the flexoelectric effect.

Equation (4) demonstrates that the polarization is essentially governed by the competition between the flexoelectric field and the depolarization field. With the stress-free boundary condition, we have $\sigma_1 = \sigma_5 = \sigma_6 = 0$ in the wall, and Eq. (4) becomes

$$\frac{\partial^2 P_1}{\partial x_1^2} = \frac{\left(E_1^d + E_1^f\right) g_{66} - E_2^f g_{16}}{g_{16}^2 - g_{11} g_{66}} \tag{5a}$$

$$\frac{\partial^2 P_2}{\partial x_1^2} = \frac{E_2^f g_{11} - \left(E_1^d + E_1^f\right) g_{16}}{g_{16}^2 - g_{11} g_{66}} \tag{5b}$$

where

$$g_{11} = g_{11}^C + \frac{g_A^C(\cos 4\theta - 1)}{4}, \; g_{16} = -\frac{g_A^C \sin 4\theta}{4},$$

$$g_{66} = g_{44}^C - \frac{g_A^C(\cos 4\theta - 1)}{4},$$

$$E_1^f = F_{12}^C\left(\frac{\partial \sigma_3}{\partial x_1} + \frac{\partial \sigma_2}{\partial x_1}\right) - \frac{F_A^C(\cos 4\theta - 1)}{4} \frac{\partial \sigma_3}{\partial x_1},$$

$$E_2^f = \frac{F_A^C \sin 4\theta}{4} \frac{\partial \sigma_2}{\partial x_1},$$

$$g_A^C = g_{11}^C - g_{12}^C - 2g_{44}^C, \text{ and } F_A^C = F_{11}^C - F_{12}^C - F_{44}^C.$$

The superscript C denotes the tensors in the original crystallographic coordinate of pseudocubic lattice. The indices are simplified following Voigt notation. The tensors in the rotated coordinate system as functions of the domain wall angle θ are listed in Table II in the Appendix.

Due to the electrostrictive effect, the stress distribution of the domain wall is always symmetric with respect to the domain wall center, as illustrated in Fig. 5(a). The flexoelectric fields are thus odd functions since they are proportional

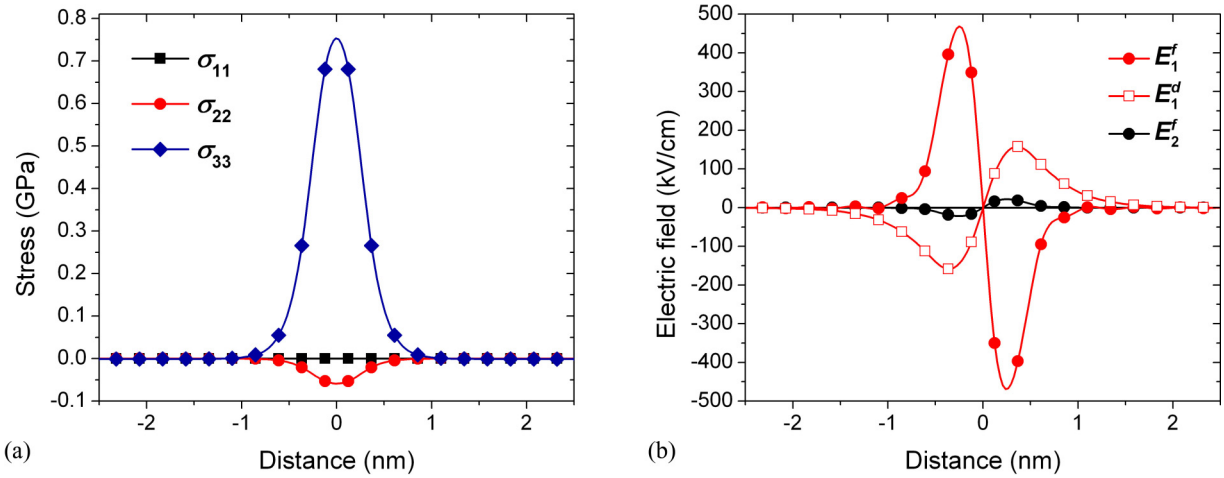

FIG. 5. (Color online) (a) Stress distribution around the domain wall with $\theta = 5\pi/12$ from the phase-field method, (b) depolarization field (E^d), and flexoelectric field (E^f) around the domain wall with $\theta = 5\pi/12$ from the phase-field method. The lines are a guide to the eye.

to the stress gradient. This feature is not limited to the pure ferroelectric but is applied to all domain walls. The depolarization and flexoelectric fields in x_1 and x_2 directions are plotted in Fig. 5(b). The flexoelectric field ${E_1}^f$ is around an order of magnitude larger than ${E_2}^f$ because the gradient of σ_{33} is much larger than that of σ_{22}. However, it is greatly weakened by the depolarization field. This explains why a larger flexoelectric field cannot induce larger P_1 as compared to P_2. The flexoelectric and depolarization fields at the domain wall are thus the key factors determining the magnitude of the flexoelectricity-induced Néel and Bloch type polarization components.

From LGD analytical theory, we also derived an approximate expression of P_1, $P_1(x_1,\theta) \approx \varepsilon_0\varepsilon_b P_s^2 \frac{2F_{12}}{R_c} \frac{Q_{11}+Q_{12}}{s_{11}+s_{12}} \frac{\sinh(x_1/R_c)}{\cosh^3(x_1/R_c)}$, where R_c is the correlation radius, $F_{12} = F_{12}^c + \frac{1}{2}\sin^2(2\theta)(F_{11}^c - F_{12}^c - F_{44}^c)$, and P_S is the spontaneous polarization far from the domain wall (see the Appendix for details of derivations). The odd distribution of $P_1(x_1,\theta) \propto \frac{\sinh(x_1/R_c)}{\cosh^3(x_1/R_c)}$ is in agreement with the phase-field simulation result shown in Fig. 3(a). The angular dependence of the maximal value $P_1^{\max}(\theta) \propto F_{12}$ also agrees qualitatively with the polar plot [Fig. 4(d)]. Due to the coupling with P_1, the analytical expression for P_2 is difficult to derive. With an artificial condition of $P_1 \equiv 0$, a previous study [5] obtained that $P_2^{\max}(\theta) \propto \sin(4\theta)(F_{44}^c - F_{11}^c - F_{12}^c)$. However, as shown in our phase-field results and first-principles calculations, P_1 and P_2 have similar magnitudes. Therefore P_1 should not be neglected, and this expression should be taken qualitatively.

From the discussion above, we conclude that the P_1 component cannot be entirely suppressed, and it has the same magnitude as P_2. Furthermore, the existence of the Néel feature is not limited to pure ferroelectric domain walls, i.e., it can be a general phenomenon that is also present in other kinds of domain walls. For example, in $SrTiO_3$ twin walls, the polarization is induced by the so-called *roto-flexo* field [20,21]. All four kinds of domain walls discussed in Ref. [20] exhibit nonzero P_1, which is greatly suppressed by the depolarization field in each case. The existence of polar domain walls in $SrTiO_3$ is confirmed by both resonant ultrasound spectroscopy [22] and resonant piezoelectric spectroscopy [23].

Since the depolarization field only exists in x_1 direction, one may expect larger P_2 or P_3 from the flexoeletric effect in certain domain wall configurations. With the flexoelectric coefficient F of the order of $\sim 10^{-11}$ $C^{-1}m^3$, stress σ at the wall of ~ 1 GPa, domain wall width of ~ 1 nm, the polarization induced by flexoelectric effect at the wall is estimated to be ~ 1 $\mu C/cm^2$. For example, in $SrTiO_3$, P_3 in the hard antiphase boundaries and P_2 in hard twins can reach as high as several $\mu C/cm^2$ due to the large gradients of σ_{33} and σ_{22} [20,21,24]. The flexoelectric effect thus enables us a new way to control electric polarization rotation from domain wall engineering. By further manipulating the density, the domain wall can be used to tune piezoelectricity.

IV. CONCLUSIONS

In conclusion, we have developed a phase-field model of ferroelectric domains with flexoelectric effects. Both phase-field model and first-principles calculations predict that the classical Ising ferroelectric domain walls also possess both Néel-like and Bloch-like features. We demonstrate that the additional components are produced by the flexoelectric effect. The additional polarization components are more than two magnitudes smaller than the Ising component and show an antiferroelectriclike distribution at the domain wall. The chirality of Néel component is independent of domain wall orientation, while the Bloch chirality is not. Since the Néel component is induced by stress inhomogeneity at the domain walls, its existence is a general phenomenon, and its magnitude is determined by the competition between flexoelectric and depolarization effects.

ACKNOWLEDGMENTS

Y.G. would like to thank Dr. J. M. Hu for helpful suggestions. This work was supported by the U S National Science Foundation (NSF) through Grants No. DMR-0820404, No. DMR-1006541, and No. DMR-1210588. The computer simulations were carried out on the Lion-X and CyberSTAR

clusters at the Pennsylvania State University, in part supported by instrumentation (CyberSTAR Linux cluster) funded by the NSF through Grant No. OCI-0821527. A.N.M. and E.A.E. acknowledge the financial support via a bilateral State Fund of Fundamental Research of Ukraine (SFFR)-NSF project under NSF-DMR-1210588 and Grant No. UU48/002.

APPENDIX

1. Derivation of the analytical expressions for P_1

Within LGD theory, equations of state for polarization components depending only on x_1 have the form [25]:

$$2a_1P_1 + 4a_{11}P_1^3 + 2a_{12}P_2^2P_1 + 2a_{12}P_3^2P_1 + a_{16}P_2\left(3P_1^2 - P_2^2\right) - g_{11}\frac{\partial^2 P_1}{\partial x_1^2} - g_{16}\frac{\partial^2 P_2}{\partial x_1^2} - 2\left(Q_{12}\sigma_3 + Q_{12}\sigma_2\right)P_1 - Q_{26}\sigma_2P_2 = E_1^d + F_{12}\left(\frac{\partial\sigma_2}{\partial x_1} + \frac{\partial\sigma_3}{\partial x_1}\right) \tag{A1a}$$

$$2a_1P_2 + 4a_{11}P_2^3 + 2a_{12}P_1^2P_2 + 2a_{12}P_3^2P_2 + a_{16}P_1\left(P_1^2 - 3P_2^2\right) - g_{66}\frac{\partial^2 P_2}{\partial x_1^2} - g_{16}\frac{\partial^2 P_1}{\partial x_1^2} - 2\left(Q_{12}\sigma_3 + Q_{11}\sigma_2\right)P_2 - Q_{26}\sigma_2P_1 = F_{26}\frac{\partial\sigma_2}{\partial x_1} \tag{A1b}$$

$$2a_1P_3 + 4a_{11}P_3^3 + 2a_{12}\left(P_1^2 + P_2^2\right)P_3 - g_{44}\frac{\partial^2 P_3}{\partial x_1^2} - 2(Q_{11}\sigma_3 + Q_{12}\sigma_2)P_3 - Q_{44}\sigma_4P_2 = 0. \tag{A1c}$$

The right-hand side of Eq. (A1a) can be written as

$$F_{12}\frac{\partial(\sigma_2+\sigma_3)}{\partial x_1} \approx \frac{F_{12}(Q_{11}+Q_{12})}{s_{11}+s_{12}}\frac{\partial\left(-P_2^2 - P_3^2\right)}{\partial x_1}. \tag{A2}$$

Elastic stresses are

$$\sigma_1 = \sigma_5 = \sigma_6 = 0,\ \sigma_2 = \frac{s_{11}U_2 - s_{12}U_3}{s_{11}^2 - s_{12}^2},\ \sigma_3 = \frac{s_{11}U_3 - s_{12}U_2}{s_{11}^2 - s_{12}^2},\ \sigma_4 = \frac{Q_{44}\left(P_2^SP_3^S - P_2P_3\right)}{s_{44}}, \tag{A3}$$

where P_i^S is the spontaneous polarization component in x_i direction. The tensors in the rotated coordinate system are listed in Table II. Functions U_3 and U_2 are defined as

$$U_3 = Q_{11}\left(\left(P_3^S\right)^2 - P_3^2\right) + Q_{12}\left(\left(P_2^S\right)^2 + \left(P_1^S\right)^2 - \left(P_2^2 + P_1^2\right)\right) + F_{12}\frac{\partial P_1}{\partial x_1}, \tag{A4a}$$

$$U_2 = Q_{11}\left(\left(P_2^S\right)^2 - P_2^2\right) + Q_{12}\left(\left(P_3^S\right)^2 + \left(P_1^S\right)^2 - \left(P_1^2 + P_3^2\right)\right) + F_{12}\frac{\partial P_1}{\partial x_1}. \tag{A4b}$$

Thus one obtains

$$\sigma_2 + \sigma_3 = \frac{U_2 + U_3}{s_{11}+s_{12}} \equiv \frac{Q_{11}+Q_{12}}{s_{11}+s_{12}}\left(P_S^2 - P^2\right) + \frac{Q_{12}-Q_{11}}{s_{11}+s_{12}}\left(\left(P_1^S\right)^2 - P_1^2\right) + \frac{2F_{12}}{s_{11}+s_{12}}\frac{\partial P_1}{\partial x_1}, \tag{A5}$$

TABLE II. Dependence of the tensors and other coefficients on the wall rotation angle θ in the tetragonal phase (adapted from Ref. [26]).

Elastic compliance components s_{ij} in rotated coordinate system $\{x_1,x_2,x_3\}$	$s_{11} = s_{11}^C - \frac{\sin^2(2\theta)}{2}s_A^C,\ s_{12} = s_{12}^C + \frac{\sin^2(2\theta)}{2}s_A^C,$ $s_{16} = -s_{26} = -\frac{\sin(4\theta)}{2}s_A^C,\ s_{66} = s_{44}^C + 2\sin^2(2\theta)\,s_A^C,$ with $s_A^C = s_{11}^C - s_{12}^C - \frac{s_{44}^C}{2}$
Electrostriction tensor components Q_{ij} in rotated coordinate system $\{x_1,x_2,x_3\}$	$Q_{11} = Q_{11}^C - \frac{\sin^2(2\theta)}{2}Q_A^C,\ Q_{12} = Q_{12}^C + \frac{\sin^2(2\theta)}{2}Q_A^C,$ $Q_{16} = -Q_{26} = -\frac{\sin(4\theta)}{2}Q_A^C,\ Q_{66} = Q_{44}^C + 2\sin^2(2\theta)\,Q_A^C,$ with $Q_A^C = Q_{11}^C - Q_{12}^C - \frac{Q_{44}^C}{2}$
Flexoelectric field tensor components F_{ij} in rotated coordinate system $\{x_1,x_2,x_3\}$	$F_{11} = F_{11}^C - \frac{1}{2}\sin^2(2\theta)\,F_A^C,\ F_{12} = F_{12}^C + \frac{1}{2}\sin^2(2\theta)\,F_A^C,$ $F_{16} = -F_{26} = -\frac{\sin(4\theta)}{4}F_A^C,\ F_{66} = F_{44}^C + \sin^2(2\theta)\,F_A^C,\ F_{61} = 2F_{16},$ $F_{62} = 2F_{26},$ with $F_A^C = F_{11}^C - F_{12}^C - F_{44}^C$
Gradient energy coefficients g_{ij} in the rotated coordinate system $\{x_1,x_2,x_3\}$	$g_{11} = g_{11}^C - \frac{\sin^2(2\theta)}{2}g_A^C,\ g_{16} = -\frac{\sin(4\theta)}{4}g_A^C,$ $g_{66} = g_{44} + \frac{\sin^2(2\theta)}{2}g_A^C,$ with $g_A^C = g_{11}^C - g_{12}^C - 2g_{44}^C$
Landau-Devonshire coefficients a_{ij} in the rotated coordinate system $\{x_1,x_2,x_3\}$	$a_{11} = a_{11}^C - \frac{2a_{11}^C - a_{12}^C}{4}\sin^2(2\theta),\ a_{12} = a_{12}^C + 3\frac{2a_{11}^C - a_{12}^C}{2}\sin^2(2\theta),$ $a_{16} = \frac{2a_{11}^C - a_{12}^C}{2}\sin(4\theta)$

where $P_S^2 = (P_1^S)^2 + (P_2^S)^2 + (P_3^S)^2$ and $P^2 = P_1^2 + P_2^2 + P_3^2$. With the inequalities of polarization components $|P_2| \ll |P_3|$ and $|P_1| \ll |P_3|$, we can rewrite Eq. (A1a) as

$$\left(\frac{1}{\varepsilon_0\varepsilon_b} + 2a_1 + 2a_{12}P_3^2 - 2Q_{12}\frac{Q_{11}+Q_{12}}{s_{11}+s_{12}}\left(P_S^2 - P^2\right)\right)P_1 + 4a_{11}P_1^3 - \left(g_{11} + \frac{2F_{12}^2}{s_{11}+s_{12}}\right)\frac{\partial^2 P_1}{\partial x_1^2} \approx -F_{12}\frac{Q_{11}+Q_{12}}{s_{11}+s_{12}}\frac{\partial P_3^2}{\partial x_1}. \tag{A6}$$

The factor $\frac{1}{\varepsilon_0\varepsilon_b}$ comes from the depolarization field. With parameters from Table I, we can simplify the linear and gradient terms in Eq. (A6) as

$$\frac{1}{\varepsilon_0\varepsilon_b} + 2a_1 + 2a_{12}P_3^2 - 2Q_{12}\frac{Q_{11}+Q_{12}}{s_{11}+s_{12}}\left(P_S^2 - P^2\right) \approx \frac{1}{\varepsilon_0\varepsilon_b}. \tag{A7a}$$

Because in magnitude $2Q_{12}\frac{Q_{11}+Q_{12}}{s_{11}+s_{12}}(P_S^2 - P^2) \approx 2a_{12}P_3^2 \approx 2a_1 = -6 \times 10^7$ mJ/C^2 and $\frac{1}{\varepsilon_0\varepsilon_b} \approx 1.6 \times 10^{10}$ m/F, the contribution induced by depolarization field is more than 100 times larger. So the ferroelectric nonlinearity term in Eq. (A1a) can be neglected as well.

Far away from the domain wall, the derivative can be estimated as

$$\left(g_{11} + \frac{2F_{12}^2}{s_{11}+s_{12}}\right)\frac{\partial^2 P_1}{\partial x_1^2} \approx \left(g_{11} + \frac{2F_{12}^2}{s_{11}+s_{12}}\right)\frac{P_1}{R_c^2} < 10^9 P_1 \ll \frac{P_1}{\varepsilon_0\varepsilon_b}, \tag{A7b}$$

where $R_c \geqslant 0.5 \times 10^{-9}$ m is the correlation radius. Since $\frac{2F_{12}^2}{s_{11}+s_{12}}$ has the similar magnitude as $g_{11} = 5 \times 10^{-10}$ C^{-2}·m^3·J, the gradient term is at least 10 times smaller than $\frac{P_1}{\varepsilon_0\varepsilon_b}$. Thus it can be omitted as well. Eventually without losing accuracy, Eq. (A6) can be simplified as $\frac{P_1}{\varepsilon_0\varepsilon_b} \approx -F_{12}\frac{Q_{11}+Q_{12}}{s_{11}+s_{12}}\frac{\partial P_3^2}{\partial x_1}$. Thus the approximate expression for P_1 is

$$P_1 \approx -\varepsilon_0\varepsilon_b F_{12}\frac{Q_{11}+Q_{12}}{s_{11}+s_{12}}\frac{\partial P_3^2}{\partial x_1}. \tag{A8}$$

Using the approximation $P_3 \approx P_S \tanh(x_1/R_c)$ and the strong inequality $|P_2| \ll |P_3|$, we obtained

$$\begin{aligned} P_1 &\approx 2\varepsilon_0\varepsilon_b F_{12}\frac{Q_{11}+Q_{12}}{s_{11}+s_{12}}\frac{\sinh(x_1/R_c)}{\cosh^3(x_1/R_c)} \\ &\equiv \frac{\varepsilon_0\varepsilon_b}{R_c}P_S^2\left(2F_{12}^C - \sin^2(2\theta)\left(F_{44}^C + F_{12}^C - F_{11}^C\right)\right)\frac{Q_{11}+Q_{12}}{s_{11}+s_{12}}\frac{\sinh(x_1/R_c)}{\cosh^3(x_1/R_c)}. \end{aligned} \tag{A9}$$

Subscripts 1, 2, and 3 denote Cartesian coordinates x, y, and z, and Voigt's (matrix) notations are used: $a_{11} \equiv a_1$, $a_{1111} \equiv a_{11}$, $6a_{1122} \equiv a_{12}$, $g_{1111} \equiv g_{11}$, $g_{1122} \equiv g_{12}$, $g_{1212} \equiv g_{66}$, $Q_{1111} \equiv Q_{11}$, $Q_{1122} \equiv Q_{12}$, $4Q_{1212} \equiv Q_{44}$, $s_{1111} \equiv s_{11}$, $s_{1122} \equiv s_{12}$, $4s_{1212} \equiv s_{44}$, $F_{1111} \equiv F_{11}$, $F_{1122} \equiv F_{12}$, and $2F_{1212} \equiv F_{44}$. Note that different factors (either 4, 2, or 1) in the definition of matrix notations with indices 44 are determined by the internal symmetry of tensors as well as by the symmetry of the corresponding physical properties tensors (see, e.g., Ref. [27]).

2. Discussion on the sensitivity of an induced polarization component on various parameters

To discuss the sensitivity of the calculated polarization on the parameters used in the phase-field simulations, we divide the parameters into three groups: the parameters related to the thermodynamic potential, the flexoelectric coupling coefficients, and the background dielectric constant.

(i) The parameters related to the thermodynamic potential include the Landau-Devonshire coefficients, the elastic stiffness constants, gradient energy coefficients, and electrostrictive constants. Actually there are at least four sets of parameters available for the thermodynamic potential of $BaTiO_3$ [10,28–30]. In our phase-field simulation, we chose the parameters from J. J. Wang *et al.* [10]. As demonstrated in his paper, this set of parameters can reproduce the spontaneous polarization, dielectric constant, temperature-electric field phase diagram, and piezoelectric coefficients. In addition, this set of parameters was shown to be the best in reproducing the electric field induced tetragonal to orthorhombic ferroelectric transition [31].

(ii) The flexoelectric coefficients from the experiment measurement are three orders of magnitude larger than the calculated values [32]. The disagreement may come from different boundary conditions used [33], surface flexoelectric effect, dynamic flexoelectric effect, etc. [32]. It is more reasonable to use the calculated values from first principles. In order to evaluate the sensitivity of the calculated results on the values of flexoelectric coefficients, we made a comparison

TABLE III. The flexoelectric coefficients.

	f_{11}	f_{12}	f_{44}	Ref.
Set #1 ($Ba_{0.5}Sr_{0.5}TiO_3$)	59.86 nC/m	38.81 nC/m	0.526 nC/m	[34]
Set #2 ($BaTiO_3$, used in the main text)	0.150 nC/m	−5.463 nC/m	−1.904 nC/m	[9]

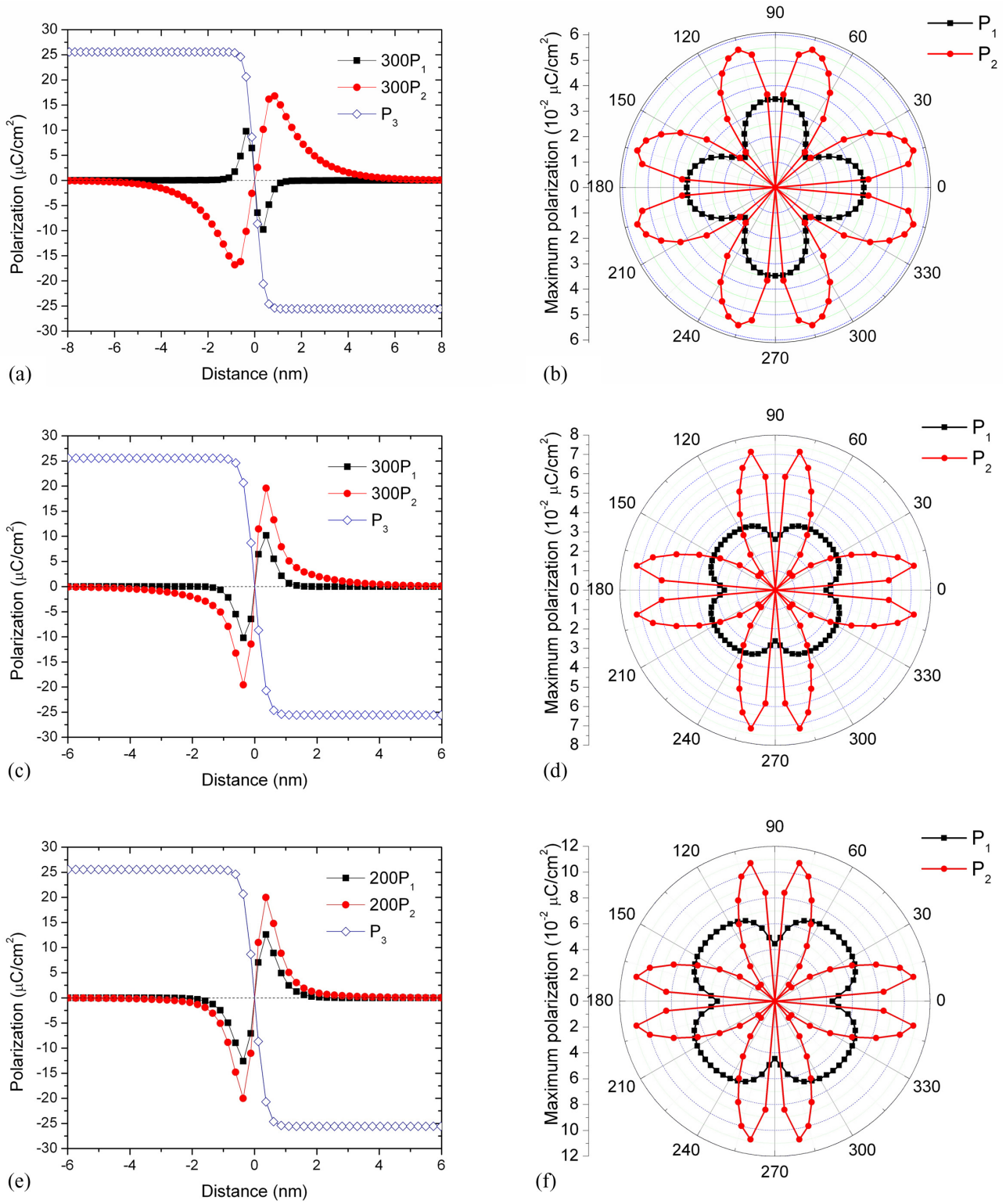

FIG. 6. (Color online) Polarization profiles with $\theta = \pi/12$ and the maximum values of P_1 and P_2 components as a function of domain wall orientation (θ is the angle between the domain wall and the [010] direction). (a), (b) Calculated with flexoelectric coefficients set #1 and background dielectric constant of 7.35. (c), (d) Calculated with flexoelectric coefficients set #2 and background dielectric constant of 7.35. (e), (f) Calculated with flexoelectric coefficients set #2 and background dielectric constant of 45.

using two sets of flexoelectric coefficients (Table III) [9,34]. Although, both sets of flexoelectric coefficients are from first-principles calculations, they are quite different in terms of magnitude and sign. As shown in Fig. 6(a)–6(d), although the flexoelectric effect induced polarization components, namely P_1 and P_2, are dependent on the flexoelectric coefficients in terms of profiles and anisotropy, they still exist. The magnitudes of both induced polarization components do not

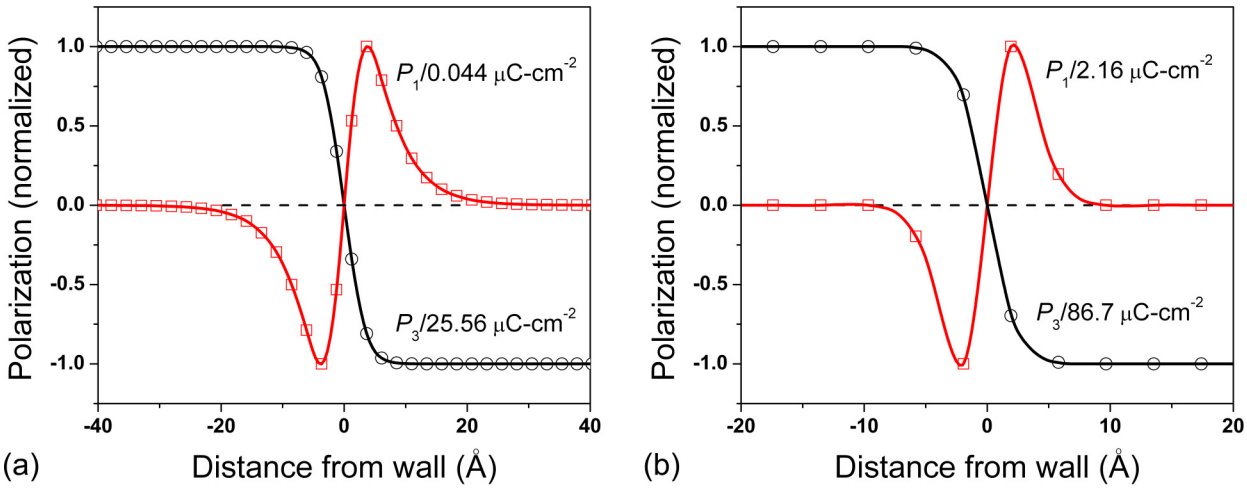

FIG. 7. (Color online) Domain wall profiles of (a) $BaTiO_3$ calculated from phase-field simulation (this work) and (b) $PbTiO_3$ calculated from first principles (reproduced from D. Lee *et al.* [3]). P_1 in (a) corresponds to P_n (normal) in (b), and P_3 in (a) corresponds to P_z in (b).

change much despite the huge difference between the two sets of flexoelectric coefficients. The profile of P_1 clearly flipped, which is mainly due to the sign change of f_{12}.

(iii) As demonstrated in Eqs. (4) and (5), the depolarization field E^d has a strong effect on the induced polarization. Therefore, the background dielectric constant, which determines the strength of the depolarization electric field, is another important parameter. In order to discuss the sensitivity of induced polarization on the background dielectric constant, we need to start from the two contributions to the polarization of a ferroelectric material: (a) the critical displacements of ions (responsible for enhanced dielectric constant and spontaneous polarization), and (b) all the other polar distortions. The background dielectric constant is from the latter contribution [14]. So we chose two quite different values, listed in Table I. One is 7.35, which is essentially from room temperature infrared and Raman reflectivity data [35]. The other is 45, taken from Rupprecht and Bell's work [12]. As pointed out by Ref. [12], the background dielectric constant "consists of contributions from the electric polarizability, temperature-independent optically active lattice vibrations, and a dominant term stemming from the finite frequency of the temperature-dependent soft mode in the limit of infinite temperature." Thus the value 7.35, which is from the optical modes only, is not sufficient. However, the simulation results do not show much difference as we compare Figs. 6(c)–6(f). The Néel and Bloch features still exist and maintain their anisotropy. Only the magnitudes of both components are about two times larger than our previous calculations. That is because the increased background dielectric constant weakened the depolarization field.

From the above analysis, we can conclude that the induced polarization components calculated from phase-field simulation do depend on the parameters. Their anisotropy is dependent on the flexoelectric coefficients. And their magnitude is dependent on both the flexoelectric coefficients and the background dielectric constant. But the general physical phenomenon, flexoelectric effect-induced two new polarization components at the 180° domain wall, is not sensitive to the parameters. As demonstrated by our analysis, the Néel-like (P_1) and Bloch-like (P_2) polarization components are essentially dominated by Eq. (5). Both the flexoelectric field and the depolarization field are functions of polarization. Therefore, only in some very special cases, for example $F_A^C = g_A^C = g_{44}^C = 0$, there are no P_1 and P_2 with any domain wall orientation. To prove the reliability of our calculations, we also compared our simulation result of $BaTiO_3$ with Lee's DFT calculations of $PbTiO_3$ [3], as shown in Fig. 7. Although the materials and the computational methods are quite different, the polarization profiles are very similar.

3. Computational details for first-principles calculations

We performed first-principles calculations using density functional theory as implemented in the Vienna *Ab initio* Simulation Package [36]. We used the projector-augmented wave method [37,38] with an energy cutoff of 400 eV and generalized gradient approximations with Perdew-Burke-Ernzerhof pseudopotentials revised for solids (PBEsol) [39]. Ba $5s$, $5p$, and $6s$ electrons, Ti $3s$, $3p$, $3d$, and $4s$ electrons, and O $2s$ and $2p$ electrons were treated as valence states. We relaxed the atom positions along with the length of the lattice vector normal to the domain wall plane using the conjugate gradient algorithm [40] until the residual forces were smaller than 0.01 eV/Å. The Born effective charge tensors were calculated with density functional perturbation theory. A $1 \times 9 \times 9$ Monkhorst-Pack k-mesh is used for $(100)_C$ domain walls, and a $1 \times 3 \times 7$ k-mesh is used for $(140)_C$ domain wall. The accuracy has been checked to be sufficient.

[1] S. M. Kogan, Sov. Physics-Solid State **5**, 2069 (1964).
[2] J. Padilla, W. Zhong, and D. Vanderbilt, Phys. Rev. B **53**, R5969 (1996).
[3] D. Lee, R. K. Behera, P. Wu, H. Xu, Y. L. Li, S. B. Sinnott, S. R. Phillpot, L. Q. Chen, and V. Gopalan, Phys. Rev. B **80**, 060102(R) (2009).

[4] A. Angoshtari and A. Yavari, J. Appl. Phys. **108**, 084112 (2010).
[5] P. V. Yudin, A. K. Tagantsev, E. A. Eliseev, A. N. Morozovska, and N. Setter, Phys. Rev. B **86**, 134102 (2012).
[6] L. Q. Chen, Annu. Rev. Mater. Res. **32**, 113 (2002).
[7] L. Q. Chen and J. Shen, Comput. Phys. Commun. **108**, 147 (1998).
[8] E. A. Eliseev, A. N. Morozovska, M. D. Glinchuk, and R. Blinc, Phys. Rev. B **79**, 165433 (2009).
[9] R. Maranganti and P. Sharma, Phys. Rev. B **80**, 054109 (2009).
[10] J. J. Wang, P. P. Wu, X. Q. Ma, and L. Q. Chen, J. Appl. Phys. **108**, 114105 (2010).
[11] J. Hlinka and P. Márton, Phys. Rev. B **74**, 104104 (2006).
[12] G. Rupprecht and R. O. Bell, Phys. Rev. **135**, A748 (1964).
[13] A. G. Khachaturyan, *Theory of Structural Transformations in Solids* (Dover Publications Inc., Mineola, New York, 2008), p. 576.
[14] A. K. Tagantsev, Ferroelectrics **375**, 19 (2008).
[15] Y. Zheng and C. H. Woo, Appl. Phys. A **97**, 617 (2009).
[16] F. Jona and G. Shirane, *Ferroelectric Crystals* (Dover Publications Inc., Mineola, New York, 1993).
[17] B. Meyer and D. Vanderbilt, Phys. Rev. B **65**, 104111 (2002).
[18] R. K. Behera, C. Lee, D. Lee, A. N. Morozovska, S. B. Sinnott, A. Asthagiri, V. Gopalan, and S. R. Phillpot, J. Phys.: Condens. Matter **23**, 175902 (2011).
[19] W. Ma, Phys. Status Solidi B **245**, 761 (2008).
[20] A. N. Morozovska, E. A. Eliseev, M. D. Glinchuk, L. Q. Chen, and V. Gopalan, Phys. Rev. B **85**, 094107 (2012).
[21] A. N. Morozovska, E. A. Eliseev, S. V. Kalinin, L. Q. Chen, and V. Gopalan, Appl. Phys. Lett. **100**, 142902 (2012).
[22] J. F. Scott, E. K. H. Salje, and M. A. Carpenter, Phys. Rev. Lett. **109**, 187601 (2012).
[23] E. K. H. Salje, O. Aktas, M. A. Carpenter, V. V. Laguta, and J. F. Scott, Phys. Rev. Lett. **111**, 247603 (2013).
[24] A. N. Morozovska, Y. Gu, V. V. Khist, M. D. Glinchuk, L. Q. Chen, V. Gopalan, and E. A. Eliseev, Phys. Rev. B **87**, 134102 (2013).
[25] E. A. Eliseev, A. N. Morozovska, G. S. Svechnikov, P. Maksymovych, and S. V. Kalinin, Phys. Rev. B **85**, 045312 (2012).
[26] A. N. Morozovska, R. K. Vasudevan, P. Maksymovych, S. V. Kalinin, and E. A. Eliseev, Phys. Rev. B **86**, 085315 (2012).
[27] J. F. Nye, *Physical Properties of Cristals: Their Representation by Tensors and Matrices* (Oxford University Press, Oxford, 1985).
[28] Y. L. Wang, A. K. Tagantsev, D. Damjanovic, N. Setter, V. K. Yarmarkin, A. I. Sokolov, and I. A. Lukyanchuk, J. Appl. Phys. **101**, 104115 (2007).
[29] Y. L. Li, L. E. Cross, and L. Q. Chen, J. Appl. Phys. **98**, 064101 (2005).
[30] A. J. Bell and L. E. Cross, Ferroelectrics **59**, 197 (1984).
[31] D. J. Franzbach, Y. Gu, L. Q. Chen, and K. G. Webber, Appl. Phys. Lett. **101**, 232904 (2012).
[32] P. Zubko, G. Catalan, and A. K. Tagantsev, Annu. Rev. Mater. Res. **43**, 387 (2013).
[33] J. Hong and D. Vanderbilt, Phys. Rev. B **88**, 174107 (2013).
[34] I. Ponomareva, A. K. Tagantsev, and L. Bellaiche, Phys. Rev. B **85**, 104101 (2012).
[35] J. L. Servoin, F. Gervais, A. M. Quittet, and Y. Luspin, Phys. Rev. B **21**, 2038 (1980).
[36] G. Kresse and J. Furthmuller, Phys. Rev. B **54**, 11169 (1996).
[37] G. Kresse and D. Joubert, Phys. Rev. B **59**, 1758 (1999).
[38] P. E. Blochl, Phys. Rev. B **50**, 17953 (1994).
[39] J. P. Perdew, K. Burke, and M. Ernzerhof, Phys. Rev. Lett. **77**, 3865 (1996).
[40] W. H. Press, B. P. Flannery, S. A. Teukolsky, and W. T. Vetterling, *Numerical Recipes in C: The Art of Scientific Computing* (Cambridge University Press, Cambridge, 1992).